Nano Energy 37 (2017) 90–97

Contents lists available at ScienceDirect

Nano Energy

journal homepage: www.elsevier.com/locate/nanoen

Full paper

In-situ mass-electrochemical study of surface redox potential and interfacial chemical reactions of Li(Na)$FePO_4$ nanocrystals for Li(Na)-ion batteries

Xiaohe Song[a,1], Tongchao Liu[a,1], Joseph Amine[a], Yandong Duan[a], Jiaxin Zheng[a,*], Yuan Lin[a,b], Feng Pan[a,*]

[a] School of Advanced Materials, Peking University, Shenzhen Graduate School, Shenzhen 518055, People's Republic of China
[b] Institute of chemistry, Chinese Academy of Science, Beijing 100080, People's Republic of China

ARTICLE INFO

Keywords:
Lithium ion battery
Surface redox potential
Electrochemical quartz crystal microbalance
Density functional theory
Interfacial structure

ABSTRACT

In this work, an in-situ experimental mass-electrochemical investigation of the $LiFePO_4$ (LFP) and $NaFePO_4$ (NFP)electrolyte interfacial chemical reactions and surface redox potential is achieved by adopting electrochemical quartz crystal microbalance (EQCM) to monitor the mass change trend. In organic electrolyte, LFP (NFP) cathode's mass decreases/increases during the charge/discharge process because of deintercalation/intercalation of Li (Na) ions, which is an normal phenomenon which is generally known. However, the mass-potential curve for LFP nanocrystals in aqueous electrolyte show an anomalous mass change interval (AMCI) around 3.42 V (vs. Li/Li^+) where the cathode's mass increase in the charging process and mass decrease in the discharging process, which doesn't obey the normal law of mass change. Through density functional theory (DFT) calculations, we gain a microscopic picture of the solid-liquid interface structure with a reconstructed LFP (010)/H_2O and NFP (010)/H_2O interface. Taken together, it's concluded that the surface redox potential of LFP is around 3.31 V, which is lower than the bulk potential (3.42 V) and the desolvation/solvation rate of surficial Li-ion is lower than the bulk Li-ion diffusion rate. While for NFP, it's surface redox potential is almost the same as the bulk one.

1. Introduction

Interfacial chemistries often play a key role in the performance of lithium ion batteries [1–4], it is important to getting deep insight of the properties of electrode/electrolyte interface. Nevertheless, due to the electrode surface's liquidity, irregular surface, and complex solid electrolyte interphase (SEI) [5,6], direct investigation of interfacial structures of electrode materials in electrolytes remains challenging and attractive. Masaaki Hirayama et al. studied the in-situ dynamic structural changes at $LiMn_2O_4$/electrolyte interface during electrochemical cycling by using surface X-ray diffraction (SXRD) technique, and it is found that the surface structural changes commence with the formation of an electric double layer, which is followed by surface reconstruction when a voltage is applied in the first charge process [7]. By in-situ total reflection fluorescence X-ray absorption spectroscopy, Yamamoto et al. studied the effects of the electronic structure at the electrode/electrolyte interface on the cyclic performance of the cathode materials ($LiCoO_2$ and $LiFePO_4$) [8]. They found that the reduction of Co ions at the electrode/electrolyte interface happens during cycling in a $LiCoO_2$ thin-film electrode in an organic electrolyte, with subsequent irreversible changes after cycling. While for the $LiFePO_4$ thin-film electrode, the electronic structure at the electrode/electrolyte interface was stable and reversible upon electrolyte immersion with subsequent cycling.

For $LiFePO_4$, there is no complex SEI when performed in the organic electrolyte system [9–11]. In addition, the carbon coating also does not block the electrolyte from directly contacting with the LFP surfaces [11,12]. Therefore LFP/electrolyte interface is simple, which makes it an ideal model for experimental and theoretical investigations of the electrode's solid-liquid interface, and some efforts has been made on this subject. Wang et al. studied the surface properties of LFP in vacuum by using DFT calculations, they found (010) surface, named LFP (010), to be the most energetically favorable surface [13], and the surface redox potential of (010) surface is calculated to be around 3.0 V, which is 0.5 V lower than the bulk potential(3.5 V). Lots of experiments also demonstrated (010) surface to be the mostly exposed one [14,15]. Zheng et al. Reported that LFP nanocrystals in aqueous electrolyte presented an ultra-high rate capability and ascribed it to the

* Corresponding authors.
E-mail addresses: zhengjx@pkusz.edu.cn (J. Zheng), panfeng@pkusz.edu.cn (F. Pan).
[1] These authors contributed equally to this work.

http://dx.doi.org/10.1016/j.nanoen.2017.05.019
Received 4 February 2017; Received in revised form 8 May 2017; Accepted 8 May 2017
Available online 10 May 2017

electrode/electrolyte solid-liquid interface [4]. By adopting single-particle electrode model, Hu et al. found that the interfacial rate constant of chemical reaction in aqueous electrolyte is one order higher than in organic electrolyte [16]. Similar as LFP, olivine phase $NaFePO_4$ (NFP) is an important promising cathode material for sodium ion batteries (SIBs) with a high theoretical capacity of 154 mA h g^{-1} [17]. Olivine phase NFP was typically synthesized via an ion exchange method by electrochemical insertion of sodium ions into chemical or electrochemical delithiated $FePO_4$ [18,19]. There is still few studies about the solid-liquid interfacial properties of NFP, it's believed that comparative study between LFP and NFP will provide a more comprehensive understanding of LFP's [20] electrochemical performance.

Electrochemical quartz crystal microbalance (EQCM) is highly sensitive to the mass and morphology change during the electrochemical reactions and has been widely employed to investigate film growth, porous materials, protein denaturation, and so on [21–24]. EQCM was recently used to in-situ study cathode materials of LIBs [25–27]. Using electrochemical quartz crystal admittance (EQCA), a technique similar to EQCM, Levi et al. found exceptionally high selectivity of Li-ions insertion into $FePO_4$ as compared to that of Na-ions in mixed aqueous electrolyte solutions of lithium and sodium sulfates [25]. Shpigel et al. studied $LiMn_2O_4$ by EQCM combined with in situ hydrodynamic spectra, which enables a comprehensive understanding of how ion insertion/extraction affects the structure of the porous electrode in contact with solutions on a mesoscopic scale [26]. However, the detailed direct experimental observation of LFP's electrode/electrolyte interfacial chemical reactions during cycling is still in lack.

In this work, EQCM and DFT calculation are combined to study the interfacial properties of LFP. First, EQCM test is applied to monitor the mass change of the cathode during the charge/discharge process. It's found that both LFP and NFP nanocrystals, as the cathode material with organic electrolyte, have the normal monotonic mass-charge curves that the cathode's mass decreases as the decrease/increase in the charge/discharge process. In aqueous electrolytes, LFP nanocrystals show a mass-potential curve with an anomalous mass change interval (AMCI) appearing around 3.42 V (vs. Li/Li^+) where the charge (Δq) and the mass (Δm) decrease/increase synchronously in the charging/discharging process, while for NFP the mass-potential curve is normal. Through DFT calculations, we get a microscopic picture of the solid-liquid interfacial chemical reactions and the surface redox potential of LFP and NFP nanocrystals. Taken together, we concluded that the surface redox potential of LFP is around 3.31 V, which is lower than the bulk potential 3.42 V and the desolvation/solvation rate of surficial Li-ion is lower than the bulk Li-ion diffusion rate.

2. Materials and methods

2.1. Synthesis of $LiFePO_4$ and $NaFePO_4$ nanocrystals

The $LiFePO_4$ particles with mean size of 100 nm and 40 nm were synthesized by reflux route in ethylene glycol solution under atmospheric pressure. For these two kinds of particles, $FeSO_4{\cdot}7H_2O$, H_3PO_4, and $LiOH{\cdot}H_2O$ were used as starting materials in a molar ratio of 1:1.5:2.7 and ethylene glycol (EG) was applied as solvent. For the synthesis of 100 nm $LiFePO_4$, $FeSO_4$ solution was slowly introduced to the LiOH solution under stirring, and then H_3PO_4 solution was added into the mixture. For the synthesis of 40 nm $LiFePO_4$, H_3PO_4 solution was slowly introduced to the LiOH solution under stirring, and then $FeSO_4$ solution was added into the mixture. After well stirring, the mixture of two syntheses was heated at reflux condition for 10 h under Ar atmosphere. The resulting suspension was washed several times with water and ethanol. $NaFePO_4$ was prepared by electrochemical delithiation from $LiFePO_4$. The specific scheme was that $LiFePO_4$ was charged to 0.7 V at 0.5 C and then maintained the voltage at 0.7 V about 1 h in aqueous electrolyte or organic electrolyte, which ensured that lithium ions are extracted out from $LiFePO_4$ completely, and the pure $FePO_4$ were formed. After they were washed by water or DMC several times, the cells were put into 0.5 M Na_2SO_4 solution as an aqueous electrolyte or 1 M $NaClO_4$ dissolved in EC/DMC solution as an organic electrolyte, respectively. The pure $FePO_4$ was discharged to −0.4 V at 0.1 C first, then charged and discharged in the voltage range of −0.4–0.7 V (vs. Ag/AgCl) at 0.2 C several times to form $NaFePO_4$.

2.2. Electrochemical quartz crystal microbalance apparatus

For the EQCM technique, quartz crystal act as mass sensors to in situ monitor the mass variation of materials. It can be widely used under vacuum, gas phase or liquid environments. The related mass change (Δm) could be highly precisely detected according to the resulting frequency change (Δf) of the quartz crystal. The frequency change (Δf) and the mass change (Δm) obey the Sauerbrey equation [28].

$$\Delta f = -C_f \Delta m$$

In this equation, C_f is the sensitivity factor. The EQCM test was performed on an electrochemical workstation (CHI 420C, Shanghai Chenhua) and a special electrolytic cell as shown in Fig. S1 is employed. The gold electrode, platinum electrode, and saturated calomel electrode (SCE) used as working electrode, counter electrode, and reference electrode, respectively. The quartz crystals were sputtered with gold, and the frequency of the sputtered quartz crystals were found to be 8 MHz. The surface area of gold electrode available for loading the samples was 0.196 cm^2. The EQCM experiments were performed at a scan rate of 10 mV/s in the voltage range of −0.2–0.7 V for $LiFePO_4$ and −0.4–0.7 V for $NaFePO_4$ using a standard three-electrode configuration. The front electrode of the quartz crystal acting as the working electrode, a Ag/AgCl electrode was used as the reference electrode and the platinum electrode was used as the counter electrode. In this text, we convert all the potentials (vs SCE) to potentials (vs Li/Li^+) for comparison more conveniently.

2.3. Definition of mass-potential and mass-charge curves detected EQCM

As shown in Fig. 1a, both the potential and charge quantity (in the unit of mole electrons) vary gradually during the discharge/charge process, where the mass change are detected by using EQCM and the corresponding electrons transfer and the current change is monitored by cyclic voltammetry (CV). The mass change as a function of redox potential and the corresponding integrated charge quantity are defined as mass-potential and mass-charge curve, respectively. Ordinarily, as the cathode material with organic electrolyte, LFP (NFP) cathode's mass decreases/increases during the charge/discharge process because of deintercalation/intercalation of Li (Na) ions. During the discharge/charge process, every mole Li (Na)-ions transfer into/out of the electrode corresponds to a mole electrons transferring into/out of. For example, LFP cathode's mass change monotonically as a function of the charge quantity with the theoretical slope of 6.94 g mol^{-1}, because the atomic mass of Li is 6.94. For the same reason, NFP's mass-charge has theoretical slope of 22.99 g mol^{-1}. But at some times, due to the side reactions at the solid-liquid interface or interface structure changes, the slope of the mass and the charge doesn't obey this law. Thus the relationship between mass variation Δm and the charge variation Δq during charge/discharge process could provide detailed information about electrode/electrolyte interface.

2.4. DFT calculations method

All calculations are performed with the Vienna DFT simulation package (VASP) [29,30], using the plane-wave projector-augmented

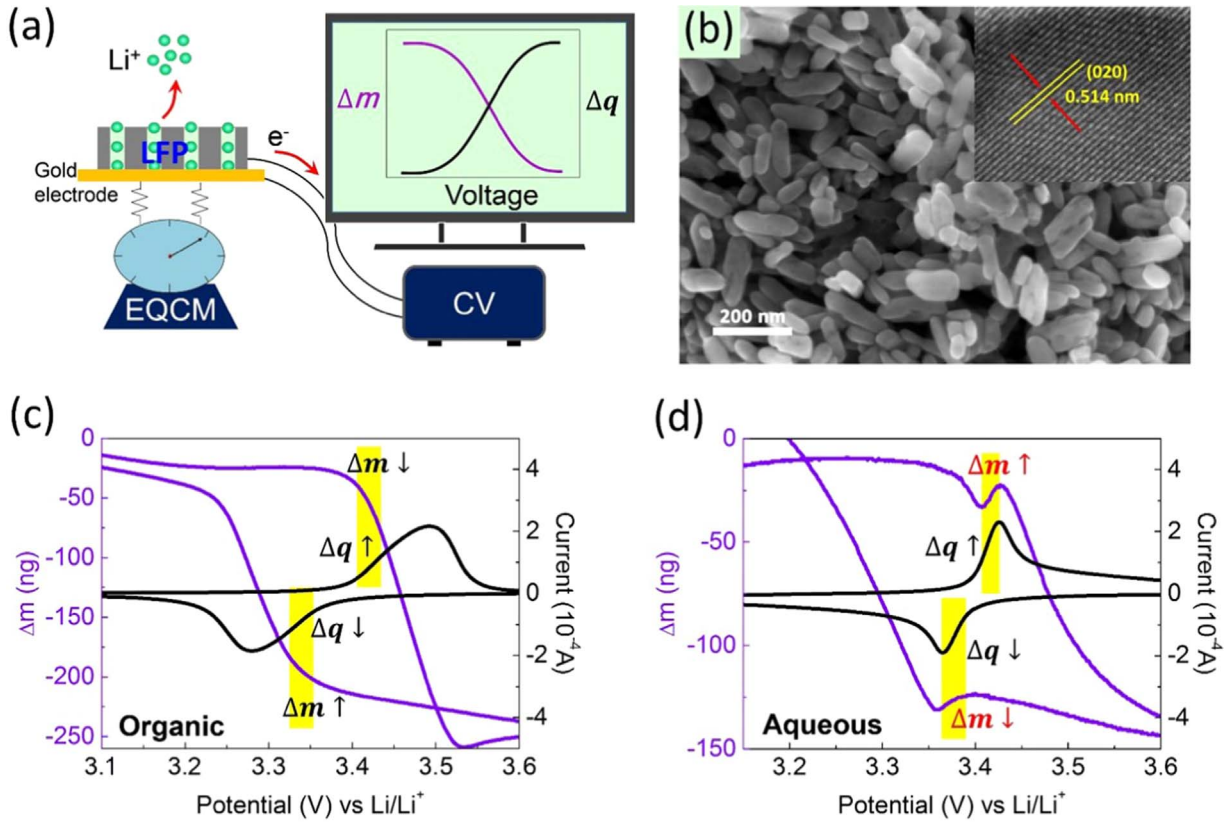

Fig. 1. (a) The schematic of the charging process of $LiFePO_4$ electrode in an EQCM apparatus, the picture in the right-top corner illustrates that as the total mass (M, purple line) of the electrode monotonically decrease as the charge capacity (Q, black line) increasing. (b) Morphology of the 100 nm particle with the mostly exposed surface detected to be (010). (c) The mass-potential cure (purple line) and CV curve (black line) of $LiFePO_4$ in organic electrolyte where the mass decrease (increase) monotonically in the charging (discharging) process, as illustrated in the upper (lower) highlighted area. (d) The mass-potential cure and CV curve of $LiFePO_4$ in aqueous electrolyte where the mass increase (decrease) shows an AMCI, which is the highlighted parts of the purple curves, in the charging (discharging) process, as shown in the upper (lower) highlighted area.

wave method [31] with an energy cut-off of 450 eV. The Perdew-Burke-Ernzerhof (PBE) [32] form of the generalized gradient approximation (GGA) was chosen as the exchange-correlation potential. Considering the strong onsite Coulomb interaction (U) present in the localized 3d electrons of Fe, the PBE+U approach [33] is employed with the same U value of 4.3 eV [34] for $Li(Na)FePO_4$ and $FePO_4$. To obtain reliable optimized structures and the total energy, all the atomic positions and cell parameters are fully relaxed by use of a conjugate gradient algorithm, and optimized structures are assumed to be reached when the force on each atom is smaller than 0.03 eV/Å. A 2×1×2 k-point grid within the Monkhorst-Pack scheme is used to sample the Brillouin zone of the slabs built on the basis of an a×2b×2c supercell with the vacuum height of 17 Å. To calculate the water and EC adsorption on $LiFePO_4$ surfaces in liquid electrolyte, the solvation model was also employed. Since VASP (plane wave basis) can't handle the localized charge in a system well due to the long range screening effect, all the calculation about the desolvation energy are recalculated using Gaussian 03 package [35] (atomic orbital basis) with HF/6–31+G*(d) basis.

3. Results and discussion

3.1. Mass electrochemical tests

For the 100 nm and 40 nm LFP nano-crystals, scan electron micrograph (SEM) and transmission electron micrograph (TEM) show that the main exposed surface is (010) (Fig. 1b and S2) and the particles are carbon coated (Fig. S3). Then the$LiFePO_4$ and $NaFePO_4$ electrodes for EQCM test is prepared in the following process. First, the $LiFePO_4$ particles and acetylene black was dispersed in 1-Methyl-2-pyrrolidinone (NMP) to prepare a mushy mixture. Second, ultrasonic dispersion method was used to sufficiently disperse the mixture to achieve quasi single particle distribution, ten times of ultrasonic dispersion was performed with every time lasting five minutes. Third, the dispersed mixture was coated on the gold electrode of quartz crystals and then dried in the drying oven at 80 °C. $NaFePO_4$ electrodes were made by electrochemical delithiation of $LiFePO_4$ electrodes. The morphology of the prepared EQCM electrode is shown in Fig. S4, which shows that it is porous with the pore size commonly larger than 100 nm and the largest thickness of the stacked particles is about 800 nm. CV and mass-potential curve were obtained at a scan rate of 10 mV/s^{-1} in aqueous electrolyte and organic electrolyte. It should be noted that EQCM is sensitive to the pore size of the porous electrode. If the diameter of a pore is much smaller than the amplitude of quartz-crystal's transverse oscillation waves, the liquids in the hole will be considered as an undistinguishable part of the electrode, and then the change of the macrostructure is hard to be detected [25]. Therefore, the pore size should be large enough to clearly detect the structural change and kinetics of the interface surrounding the pores. As PVDF binder would fill the space between particles and lead to much smaller holes, the electrode in this work is binder-free and only made of a mixture of LFP nanocrystals and carbon black to make sure that the pores is as large as enough.

We first performed the EQCM test on LFP electrode in the organic electrolyte. For the 100 nm LFP nanocrystals, the mass-potential curve (Fig. 1c) shows that the total mass of the electrode monotonically decreases as during the charging (discharging) process. Second, EQCM was applied to the aqueous electrolyte system with the 100 nm LFP nanocrystals worked as cathode. As shown in Fig. 1d, mass-potential curve illustrates that the cathode's mass begins to decrease in the range

3.31–3.42 V (vs. Li^+/Li) and then increase in the range 3.42–3.44 V. After the potential reaching 3.44 V, the mass decreases monotonically until the end of the charge process. In the discharging process, the cathode's mass increases in the range 3.51–3.41 V and sequentially decrease at the range of 3.41 ~ 3.36 V. After the potential is less than 3.36 V, the mass increases monotonically until the end of charging. This AMCI in the range 3.42–3.44 V repeatedly appears in every cycle during tests. The similar mass-potential curve are also clearly observed at every charging/discharging cycle for the 40 nm LFP nanocrystals in aqueous electrolyte (Fig. S5), indicating this is a robust phenomenon for LFP nanocrystals with different particle sizes, as long as they worked as cathode in aqueous electrolytes.

We further adjusted the upper potential limits to different values. It's found that, under the upper potential limits of 3.42 V, the cathode's mass decreases monotonically from 3.31 to 3.42 V and no AMCI is observable (Fig. S6a). Next the upper potential limit is set to 3.44 V, it can be observed that when the potential increase to 3.42 V, the AMCI with the increasing mass appears after initial mass decrease (Fig. S6b). Therefore, it confirms that only when the potential is larger than 3.42 V can the AMCI appear. Because the value 3.42 V is the bulk redox potential of LFP, so we infer that the 3.31 V is the surface redox potential for LFP surface, which was laterly demonstrated.

For better understanding the AMCI, the mass-charge curves was studied. For the 100 nm LFP nanocrystals in the aqueous electrolyte, has a slope of about 11.04 g mol^{-1} during the charge process (Fig. 2a) and 11.99 g mol^{-1} during the discharge process (Fig. 2b). While for the organic electrolyte system, the slope is 6.75 g mol^{-1} during the charge process (Fig. 2c) and 6.79 g mol^{-1} during the discharge process (Fig. 2d), both values are very close to the theoretical value of 6.94 g mol^{-1}. For the 40 nm LFP nanocrystals in aqueous electrolyte, the mass-charge curve of shows a larger slope of 13 g mol^{-1} (Fig. S7a, b).

Using the same way that is applied to the LFP, the EQCM tests to 100 nm NFP nanocrystals confirmed the above calculation results. Different from LFP nanocrystals, we can see that NFP nanocrystals in both organic and aqueous electrolytes, there is no AMCI being detected on the mass-potential curve (Fig. 3). The mass begins decrease only when the potential is larger than 2.9 V, which is the bulk voltage. The mass-charge curve for NFP nanocrystals in organic electrolytes is around 25 g mol^{-1} (Fig. 4c, d), very close to the theoretical value of 22.99 g mol^{-1}. While in aqueous electrolytes, NFP nanocrystals show larger slopes of 31–33 g mol^{-1} (Fig. 4). In addition, to make clear whether the carbon black in the electrode contribute to the occurrence of AMCI, the EQCM test was further applied to the half cell with carbon black as cathode instead of LFP. As shown in Fig. S8, it revealed that the mass keeps almost constant within the potential range of LFP, meaning that carbon black contribute little to the mass change.

We integrate the internal area of CV curve (Fig. S9) under the voltage of 3.42 V to get the capacity below the normal bulk potential (i.e., the potential platform of LFP, 3.42 V) in the charge process. It can be found that the area below 3.42 V (yellow shadowed) occupies 7.6% for 100 nm and 9.8% for the 40 nm LFP nanocrystals. The later one is lager because of the larger surface areas and more surficial Li-ions of 40 nm LFP compared to the 100 nm LFP.

As indicated by all the experimental results above, the AMCI in the mass-potential curve is a unique property for LFP nanocrystals in aqueous electrolytes. As the AMCI could be detected in the aqueous system but not in the organic system, so the difference between

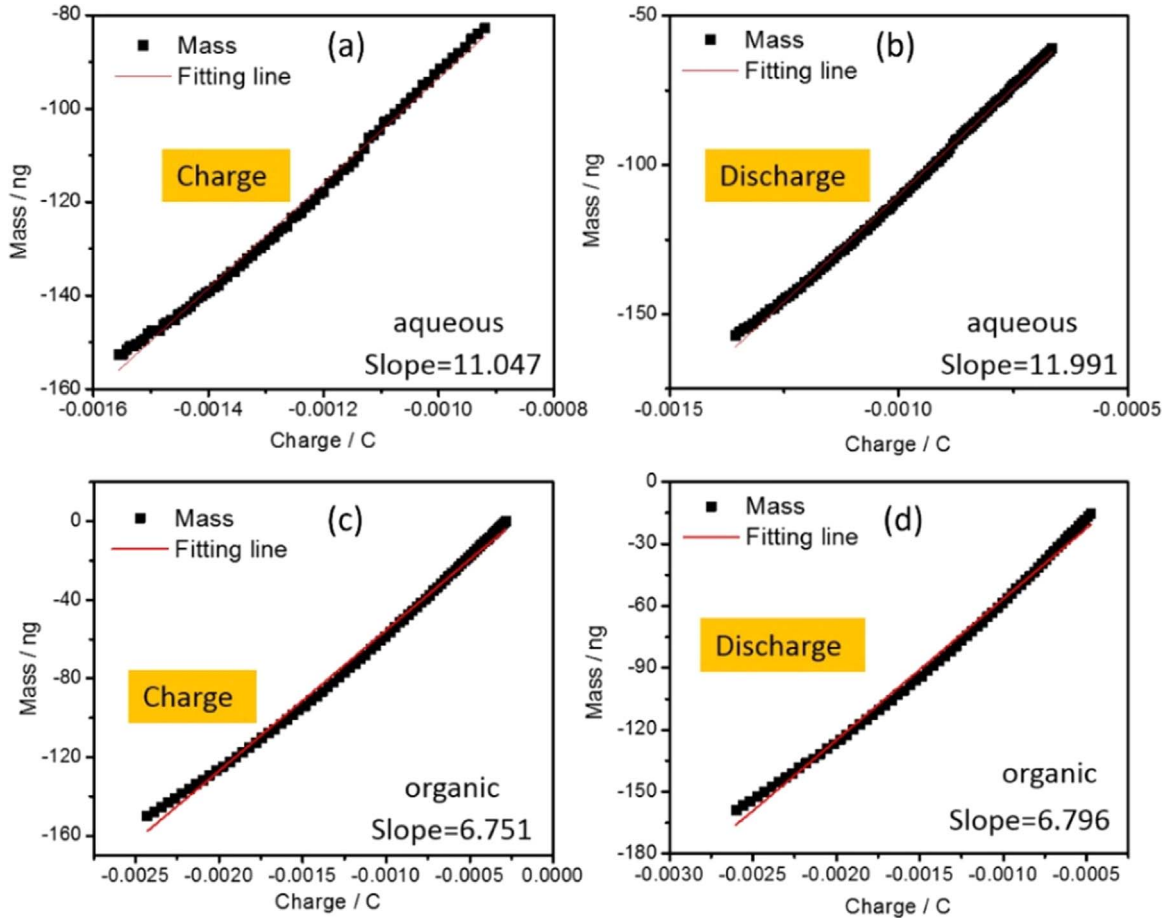

Fig. 2. (a–d) Illustrated the mass-charge curve measured by EQCM during the charge/discharge process of the 100 nm $LiFePO_4$ particles in aqueous and organic system, respectively. Slope denotes the change of mass induced by every molar electrons in the aqueous electrolyte and the organic electrolyte, respectively.

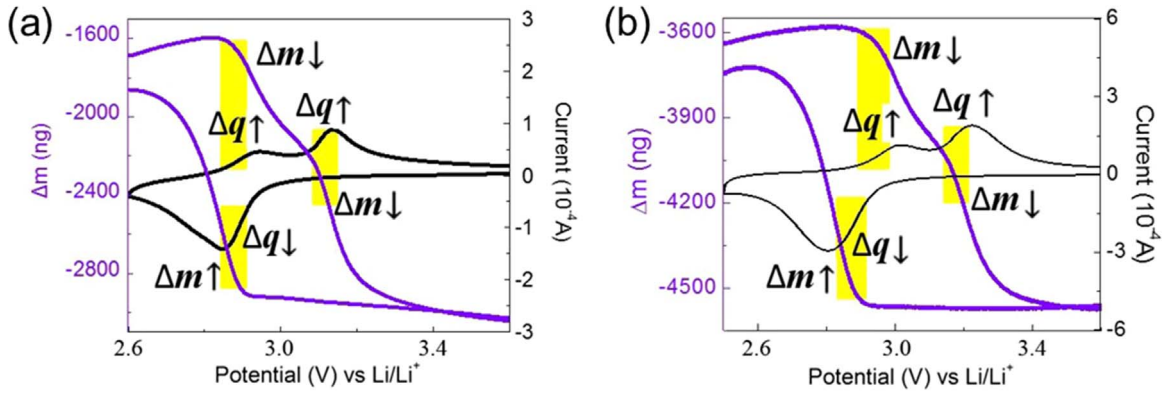

Fig. 3. The monotonic mass-potential curve and CV scan measured by EQCM for the 100 nm $NaFePO_4$ nanocrystals in (a) aqueous and (b) organic electrolytes.

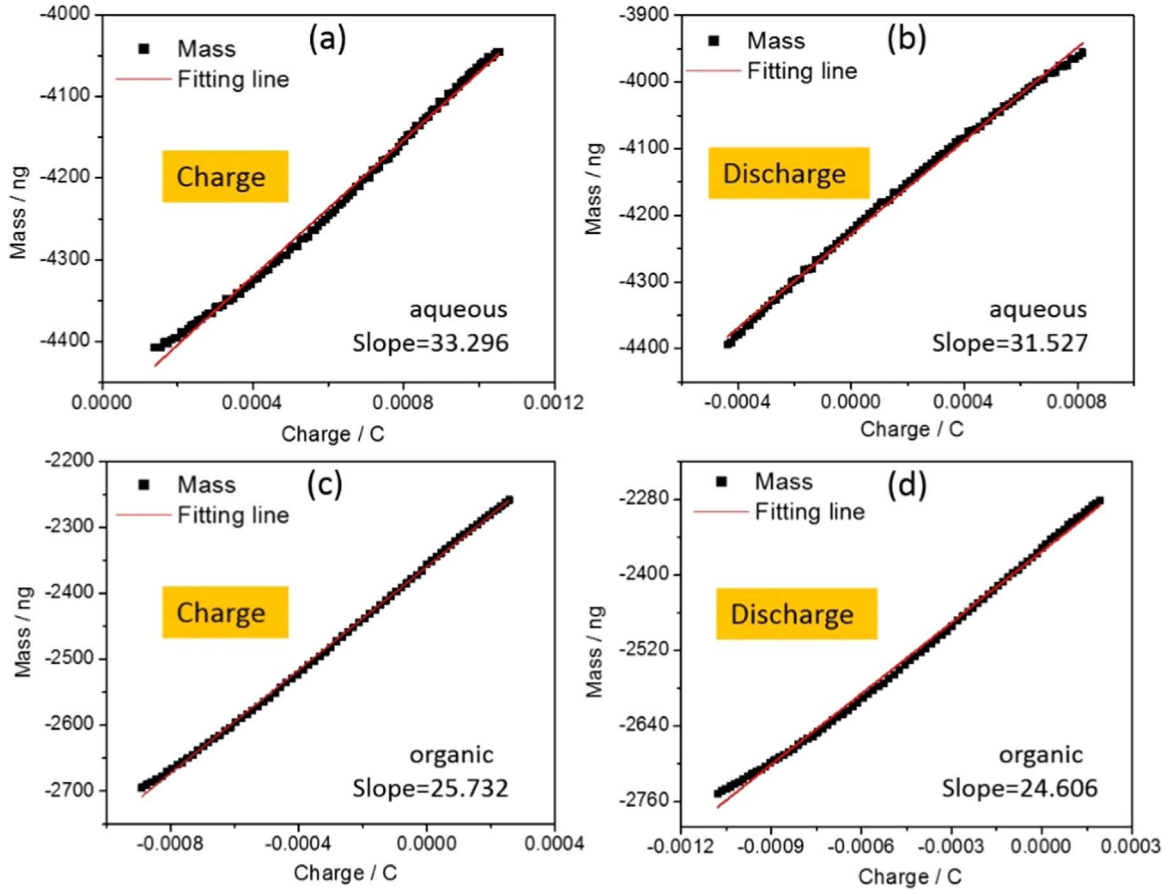

Fig. 4. (a–d) Illustrated the mass-charge curve measured by EQCM during the charge/discharge process of the 100 nm $NaFePO_4$ nanocrystals in aqueous and organic system, respectively. Slope denotes the change of mass induced by every molar electrons in the aqueous electrolyte and the organic electrolyte, respectively.

electrolytes is a cause of the AMCI. Besides, the carbon black is a suspected cause of the AMCI, because the EQCM electrodes are a mixture of $LiFePO_4$ and carbon black. Based on all the above analysis, we come to conclusion that it is the LFP and the water electrolyte that together lead to the AMCIs, and the final causes of the AMCI lie in the LFP (010)/H_2O solid-liquid interface.

3.2. DFT analysis of the structure and surficial potential of LFF (NFP)/electrolyte interface

To comprehensively understand the different mass-electrochemical performance of different working system, especially the anomalous mass change interval, DFT calculations for the LFP/electrolyte interface. As the LFP (010) surface is demonstrated to be the mostly exposed surface by both previous reports and TEM image, The following DFT analysis are all conducted on the basis of LFP (010), which is normal to the well-known [010] Li diffusion channel [33] (Fig. S11). For the pure (010) surface, the surficial Li ion (Li_{surf}) is broken from six fold to three fold and surficial Fe ion (Fe_{surf}) is broken from the six fold to five fold. For the organic electrolyte system, EC (ethylene carbonate) molecules are chosen as the contact solvent molecules, because it is the preferred solvent member in the primary solvation sheath of Li^+ despite the dominant DMC (dimethyl carbonate) presence [36]. For the LFP (010)/EC interface (Fig. 5a), every surficial Li atom, named as Li_{surf}, adsorbs only one EC molecule. While the surficial Li atom (Fe_{surf}) doesn't adsorb EC, because of the strong space steric hindrance caused by EC molecule's large size. If Li_{surf} is removed, the accompanied EC is removed too. Then the space steric hindrance on

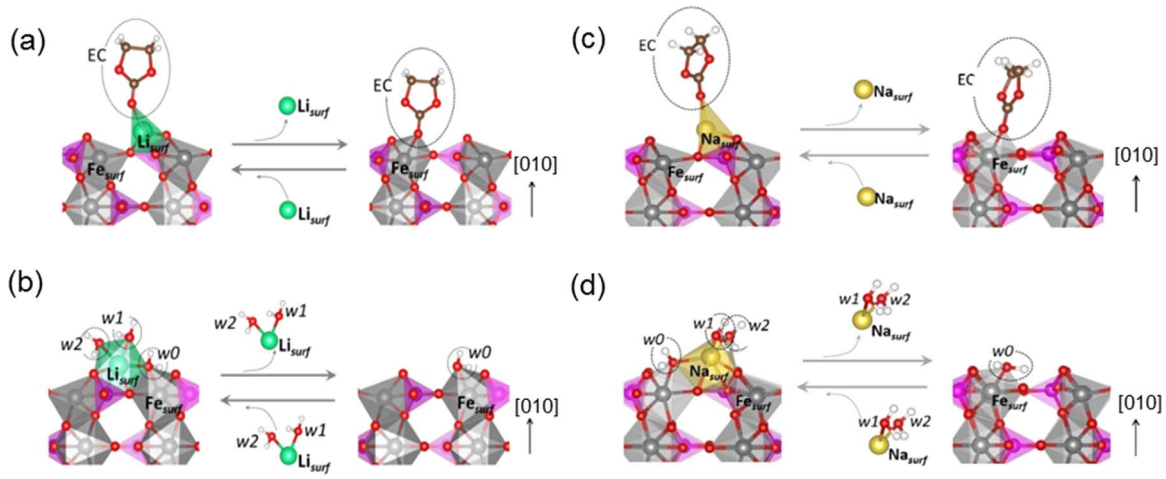

Fig. 5. (a) Scheme of the adsorption (right arrow) and desorption process (left arrow) of the surficial Li ion (Li_{surf}) on the FPO (010) surface in the EC electrolyte. The left picture shows that every Li_{surf} adsorbs one EC molecule, forming a [LiO_4] tetrahedron, and the surficial Fe-ion (Fe_{surf}) don't adsorb anything. The right picture shows the interface without Li_{surf}, where the Fe_{surf} adsorbs one EC and completes its six-fold coordination. (b) Scheme of the adsorption (right arrow) and desorption process (left arrow) of Li_{surf} on the FPO (010) surface in aqueous electrolyte. The adsorption/desorption of Li_{surf} is accompanied by two H_2O. The left picture shows that the Li_{surf} adsorbs three water molecule (ie. *w0*, *w1*, and *w2*) with *w0* shared by the surficial Fe_{surf}, and the six-fold coordination of both Li and Fe_{surf} are completed. The right picture illustrates the surface structure without Li_{surf}, where the Fe_{surf} adsorbs one H_2O and completes its six-fold coordination. (c) and (d) Scheme of the adsorption (right arrow) and desorption process (left arrow) of the surficial Na ion (Na_{surf}) on the FPO (010) surface in the EC electrolyte (c) and aqueous electrolyte (d), which are similar to the LFP cases.

this site dissappeared, allowing the Fe_{surf} adsorbs one EC. As a whole, the amounts of EC molecules adsorbing on LFP (010) keep constant and the mass change of the sufice is merely contributed by Li ions. Therefore, the mass change during the intercalated/deintercalated of Li ions has a theoretical mass-charge slope of 6.94 g mol^{-1}, which approximately equalled the experimental mass-charge slope (6.80 g mol^{-1}) for LFP in organic system (Fig. 2a, b).

While the LFP (010)/H_2O interface is reconstructed where every Li_{surf} adsorbs three water molecule, named as *w0*, *w1*, and *w2* in Fig. 5b, and *w0* is also shared by Fe_{surf}. Thus the adsorbed waters fulfill the six-fold coordination for both the Li_{surf} and the Fe_{surf}. If the Li_{surf} is removed, two of the three adsorbed water molecules *w1* and *w2* accompany, while the shared *w0* alone keeps unmoved, adsorbing on the Fe_{surf}. Therefore, the adsorption/desorption process of a surficial Li-ion could be effectively considered as a $Li^+(H_2O)_2$ group. A Li atom has light atomic mass of 6.94, while the group $Li^+(H_2O)_2$ has the atomic mass of 42.9, which drastically magnified the mass change caused by the adsorption/desorption of the surficial Li ion. This magnification effect is a key element leading to the obviously detected AMCIs around 3.42 V in the charge process and 3.40 in the discharge process, as what was highlighted in Fig. 1d. Using the same methods, we get the similar interface for the NFP nanocrystals in aqueous electrolytes (Fig. 5c, d). This LFP (010)/H_2O interface where a surficial Li atom adsorbing three water molecule is supported by the Fourier transform infrared (FTIR) spectra, which presented an additional small peak around 2800 cm^{-1} that was qualitatively in agreement with the DFT simulated modes O-H stretching mode of 2500 cm^{-1} on the basis of the LFP (010)/H_2O interface (see Section S9 in the Supporting information).

The surface redox potentials were calculated on the basis of the different structures described above. For the LFP (010) vacuum surface The surface redox potential is calculated to be 2.92 V relative to Li metal, 0.57 V lower than the calculated bulk potential 3.49 V, which is similar to the surficial redox potential reported by Wang et al. [13]. While for the LFP (010)/H_2O interface in the aqueous system, using the method discussed in the Supporting information, the surface redox potential of LFP (010)/H_2O interface is calculated to be 3.25 V, lower than the bulk value by 0.24 V, which is nearly congruent with the former inferred surficial potential (3.31 V) from the mass-potential curve. For NFP in aqueous electrolyte, the surface redox potential of $NaFePO_4$ (010)/H_2O interface is calculated to be 2.98 V, while the bulk potential is calculated to be 3.01 V. The potential difference is only 0.03 V.

3.3. Discussion about the electrochemical process the LFP/H_2O interface

For LFP in aqueous electrolyte, the above theoretical analysis illustrates that the mass change of a surficial Li ion in the adsorption/desorption process is amplified by two accompanied water and the surface redox potential (V_{surf}) is 0.24 V lower than the bulk (V_{bulk}). On the other hand, it has long been disputed that whether the rate performance of LFP is limited by Li^+-intercalation rate within the particles or the transports of Li^+ through the interface [37–39]. Previous work has identified that, with nanosized particles, the limiting step is no longer the Li+-intercalation rate within the particles but rather the transports of Li+ and electrons to or from them [40–42]. In this work, LFP nanoparticles on the electrode are well distributed coating with carbon black and they sparsely scattered on the EQCM electrode compared to the conventional LFP cathodes used in LIBs, thus it's likely that the Li ions at the interface would transfer faster than the bulk one. Accordingly, the AMCI around 3.42 V of LFP electrode in aqueous electrolyte can be explained as following.

During the charging process, the potential increases gradually and provides the external driving force for Li ion deintercalation. At the beginning of the charging process when the potential is less than V_{surf}, the surficial Li ions keep staying on the LFP (010)/H_2O interface in the form of $Li(H_2O)_2$ with two water molecules adsorbing (state 1 in Fig. 6a). As the potential increases to V_{surf} and below V_{bulk} (stage I), the surficial $Li(H_2O)_2$ gains enough force to desorb from the surface, but the bulk Li-ions keep unmoved, and hence the mass decreases. Because the desorption of a surficial Li ion is amplified by two accompanied water, the mass decrease at this stage is significantly. The final state of stage I is illustrated as state 2 with surficial Li-ions all desorbed. As the potential increases above V_{bulk}, the bulk Li ions begin deintercalation. Once a subsurface Li comes to the surface site, two H_2O molecule will come to adsorb to it, forming $Li(H_2O)_2$. Given the premise that the surficial desorption and solvation rate is slower than that of the bulk diffusion rate, the interface will soon reach a dynamic equilibrium with the end state illustrated as state 3. We called this stage as stage II. At this stage, the total mass increases due to the adsorption of water molecules. After the dynamic equilibrium process, this charging

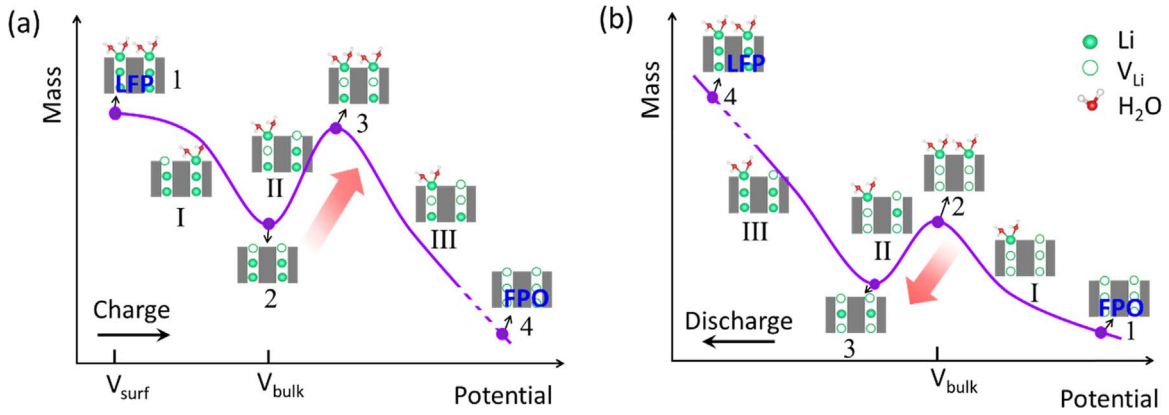

Fig. 6. (a) The simulated mass-potential curve of the charging process for $LiFePO_4$ in aqueous system at different stages. The high-lighted stage (II) illustrates that the re-adsorption of water molecule on the (010) surface leads to the abnormally mass increase. (b) The simulated mass-potential curve of the discharging process in aqueous system at different stages. The highlighted stage II illustrates that the re-desorption of water molecule on the (010) surface leads to the abnormally mass decrease.

process comes to the final stage III, where the inner Li ions deintercalate steadily and the electrode change from $Li_{1-x}FePO_4$ to $FePO_4$ (FPO).

During the discharging process (Fig. 6b), the higher the potential, the less driving force Li ions get from the electric field to move towards the cathode surface. When the potential is above V_{bulk} (stage I), Li ion couldn't intercalate into the FPO cathode. But the Li-ions could desolvate and adsorb on the FPO surface with the accompanied absorption of two H_2O, as illustrated as state 2. At this stage, the mass increases. When the potential is less than V_{bulk}, surficial Li ions begin to intercalate into the bulk LFP, and meanwhile the accompanying two H_2O desorb and move away. Given that the desolvation process and adsorption rate is slower than the intercalation rate for Li-ions, the amount of surficial $Li^+(H_2O)_2$ decreases and thus results in total mass decrease (stage II). In the following stage III, the Li ions intercalate into the bulk continuously, and the surface reaches a dynamic equilibrium, leading to continuous mass increase. According to the LFP (010)/H_2O interface above, every surficial Li ion tightly adsorb three water molecules (Section S8 in the Supporting information) and they contribute to mass of the electrode which can be detected by EQCM. For the LFP (010) surface, larger specific surface area corresponds to more surficial Li atoms and hence more adsorbed water molecules, leading to larger slope of mass-charge curve during the lithiation/delithiation process. Therefore, in aqueous electrolyte, the mass-charge curve of 40 nm LFP shows a slope of 13 g mol^{-1} which is larger than 6.75 g mol^{-1} for the 100 nm LFP.

While for NFP in aqueous electrolyte, the surface redox potential of $NaFePO_4$ (010)/H_2O interface is calculated to be 0.03 V lower than the bulk potential, and this potential difference is too small that the insertion/desertion of surficial Na ion and bulk one occur almost synchronously, therefore the mass variation of surficial Na ion would be hard to be detected separately by EQCM. On the other hand, the rate performance of NFP is usually not as good as LFP, with larger polarization and less capacity retention at high charge/discharge rate. All these reasons made NFP has a much less sensitive mass-potential curve, and thus no AMCI was observed. The well agreement between the theoretical predicted and the experimentally measured mass-potential curve and the theoretically predicted one approves that the surface redox potential of LFP is lower than the bulk potential and the desolvation/solvation rate of surficial Li-ion is lower than the bulk Li-ion diffusion rate.

4. Conclusions

We prepared the electrode that is binder-free and only made of a mixture of LFP nanocrystals and carbon black, which made sure that the pores is as large as enough. EQCM test was performed to provides a deep understanding of the solid-liquid interfacial properties of LFP and NFP nanocrystals. In organic electrolyte, LFP (NFP) cathode's mass decreases/increases during the charge/discharge process because of deintercalation/intercalation of Li (Na) ions, which is an normal phenomenon which is generally known. However, mass-potential curve for LFP nanocrystals in aqueous electrolyte show an anomalous mass change around 3.42 V (vs. Li/Li^+) where the cathode's mass increase in the charging process and mass decrease in the discharging process, which doesn't obey the normal law of mass change. Through DFT calculations, we gain a microscopic picture of the solid-liquid interface structure with a reconstructed LFP (010)/H_2O and NFP (010)/H_2O interface. For the LFP (010) vacuum surface The surface redox potential is calculated to be 2.92 V relative to Li metal, 0.57 V lower than the calculated bulk potential 3.49 V. For NFP in aqueous electrolyte, the surface redox potential of NaFePO4 (010)/H2O interface is calculated to be 2.98 V, while the bulk potential is calculated to be 3.01 V. Taken together, it's demonstrated that the surface redox potential of LFP is around 3.31 V, which is lower than the bulk potential (3.42 V). In addition, on the basis of the DFT calculated interface model, we obtain the inference that the desolvation/solvation rate of surficial Li-ion is lower than the bulk Li-ion diffusion rate.

Acknowledgements

The research was financially supported by Guangdong Innovation Team Project (No. 2013N080), ShenZhen Pea-cock Plan (Grant no. KYPT20141016105435850), and Shenzhen Science and Technology Research Grant (Nos. ZDSY20130331145131323, JCYJ20140903101617271) 01633318 and JCYJ20140903101617271).

Appendix A. Supplementary material

Supplementary data associated with this article can be found in the online version at doi:10.1016/j.nanoen.2017.05.019.

References

[1] K. Xu, Chem. Rev. 104 (2004) 4303–4418.
[2] K. Xu, Chem. Rev. 114 (2014) 11503–11618.
[3] W. Tang, X. Song, Y. Du, C. Peng, M. Lin, S. Xi, B. Tian, J. Zheng, Y. Wu, F. Pan, J. Mater. Chem. A 4 (2016) 4882–4892.
[4] J. Zheng, Y. Hou, Y. Duan, X. Song, Y. Wei, T. Liu, J. Hu, H. Guo, Z. Zhuo, L. Liu, Nano Lett. 15 (2015) 6102–6109.
[5] S. Shi, Y. Qi, H. Li, L.G. Hector Jr, J. Phys. Chem. C 117 (2013) 8579–8593.
[6] P. Verma, P. Maire, P. Novák, Electrochim. Acta 55 (2010) 6332–6341.
[7] M. Hirayama, H. Ido, K. Kim, W. Cho, K. Tamura, Ji Mizuki, R. Kanno, J. Am. Chem. Soc. 132 (2010) 15268–15276.
[8] K. Yamamoto, T. Minato, S. Mori, D. Takamatsu, Y. Orikasa, H. Tanida, K. Nakanishi, H. Murayama, T. Masese, T. Mori, H. Arai, Y. Koyama, Z. Ogumi, Y. Uchimoto, J. Phys. Chem. C 118 (2014) 9538–9543.

[9] K. Edström, T. Gustafsson, J.O. Thomas, Electrochim. Acta 50 (2004) 397–403.
[10] N. Dupré, J.-F. Martin, J. Degryse, V. Fernandez, P. Soudan, D. Guyomard, J. Power Sources 195 (2010) 7415–7425.
[11] Y. Akita, M. Segawa, H. Munakata, K. Kanamura, J. Power Sources 239 (2013) 175–180.
[12] K. Zaghib, M. Dontigny, P. Charest, J. Labrecque, A. Guerfi, M. Kopec, A. Mauger, F. Gendron, C. Julien, J. Power Sources 185 (2008) 698–710.
[13] L. Wang, F. Zhou, Y. Meng, G. Ceder, Phys. Rev. B 76 (2007) 165435.
[14] G. Chen, X. Song, T.J. Richardson, Electrochem. Solid-State Lett. 9 (2006) A295–A298.
[15] L. Wang, X. He, W. Sun, J. Wang, Y. Li, S. Fan, Nano Lett. 12 (2012) 5632–5636.
[16] J. Hu, W. Li, Y. Duan, S. Cui, X. Song, Y. Liu, J.X. Zheng, Y. Lin, P. Feng, Adv. Energy Mater. 7 (2017) 10.
[17] J. Kim, D.H. Seo, H. Kim, I. Park, J.K. Yoo, S.K. Jung, Y.U. Park, W.A.G. Iii, K. Kang, Energ. Environ. Sci. 8 (2015) 540–545.
[18] J. Lu, S.C. Chung, S.-i. Nishimura, A. Yamada, Chem. Mater. 25 (2013) 4557–4565.
[19] P. Moreau, D. Guyomard, J. Gaubicher, F. Boucher, Chem. Mater. 22 (2010) 4126–4128.
[20] K. Li, B. Zheng, J. Yan, K. Cen, Sci. Rep. 6 (2016) 39689.
[21] J.M. Griffin, A.C. Forse, W.-Y. Tsai, P.-L. Taberna, P. Simon, C.P. Grey, Nat. Mater. 14 (2015) 812–819.
[22] C. Picart, J. Mutterer, L. Richert, Y. Luo, G.D. Prestwich, P. Schaaf, J.-C. Voegel, P. Lavalle, Proc. Natl. Acad. Sci. 99 (2002) 12531–12535.
[23] K. Takada, D.J. Díaz, H.D. Abruna, I. Cuadrado, C. Casado, B. Alonso, M. Moran, J. Losada, J. Am. Chem. Soc. 119 (1997) 10763–10773.
[24] W.-Y. Tsai, P.-L. Taberna, P. Simon, J. Am. Chem. Soc. 136 (2014) 8722–8728.
[25] M.D. Levi, S. Sigalov, G. Salitra, R. Elazari, D. Aurbach, L. Daikhin, V. Presser, J. Phys. Chem. C 117 (2013) 1247–1256.
[26] N. Shpigel, M.D. Levi, S. Sigalov, O. Girshevitz, D. Aurbach, L. Daikhin, P. Pikma, M. Marandi, A. Jänes, E. Lust, Nat. Mater. 15 (2016) 570–575.
[27] Y.S. Cohen, D. Aurbach, Electrochem. Commun. 6 (2004) 536–542.
[28] G. Sauerbrey, Z. Phys. 155 (1959) 206–222.
[29] G. Kresse, J. Furthmüller, Phys. Rev. B 54 (1996) 11169.
[30] G. Kresse, J. Furthmüller, Comput. Mater. Sci. 6 (1996) 15–50.
[31] P.E. Blöchl, Phys. Rev. B 50 (1994) 17953.
[32] J.P. Perdew, K. Burke, M. Ernzerhof, Phys. Rev. Lett. 77 (1996) 3865.
[33] V.I. Anisimov, J. Zaanen, O.K. Andersen, Phys. Rev. B 44 (1991) 943.
[34] F. Zhou, C. Marianetti, M. Cococcioni, D. Morgan, G. Ceder, Phys. Rev. B 69 (2004) 201101.
[35] M.J. Frisch, G. Trucks, H. Schlegel, G. Scuseria, M. Robb, J. Cheeseman, G. Scalmani, V. Barone, B. Mennucci, G. Petersson, Gaussian 09, Gaussian, Wallingford, CT, revision A.02, 2009.
[36] A. von Cresce, K. Xu, Electrochem. Solid-State Lett. 14 (2011) A154–A156.
[37] M. Gaberscek, R. Dominko, J. Jamnik, Electrochem. Commun. 9 (2007) 2778–2783.
[38] P. He, X. Zhang, Y.G. Wang, L. Cheng, Y.Y. Xia, J. Electrochem. Soc. 155 (2008) A144–A150.
[39] G.K.P. Dathar, D. Sheppard, K.J. Stevenson, G. Henkelman, Chem. Mater. 23 (17) (2011) 4032–4037.
[40] M. Gaberscek, M. Küzma, J. Jamnik, Phys. Chem. Chem. Phys. 9 (2007) 1815–1820.
[41] J. Liu, M. Kunz, K. Chen, N. Tamura, T.J. Richardson, J. Phys. Chem. Lett. 1 (2010) 2120–2123.
[42] R. Malik, A. Abdellahi, G. Ceder, J. Electrochem. Soc. 160 (2013) A3179–A3197.

Xiaohe Song received his B.S. degree in Physics from Zhengzhou University (2013) and M.S. degree in Advanced Materials and Mechanics from the School of Advanced Materials, Peking University (2016). His primary research focuses on computational materials and energy materials.

Tongchao Liu received his B.Sc. degree in 2014 from Qingdao University, China. He is pursuing his D.Sc. degree in the School of Advanced Materials, Peking University, China. His research interests include: energy materials (battery materials, catalytic materials), nanomaterials, electrochemistry.

Joseph C. Amine is a senior student at Hinsdale Central High School in Illinois. He had summer internships at Argonne National Laboratory in Illinois, Hanyang University in Seoul of South Korea, Stanford University in California and Peking University in Shenzhen of China. Recently, he was admitted to Stanford University.

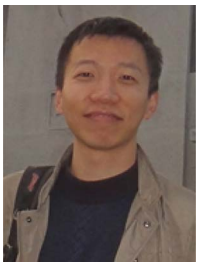

Dr. Yandong Duan received his Ph.D. degree in Physical Chemistry in Institute of Chemistry, Chinese Academy of Sciences in 2013, followed by two years postdoctoral research at Peking University. After that, he joined the School of Advanced Materials at Peking University Shenzhen Graduate School as a Research Assistant. His current interest includes the synthesis and characterization of nanomaterials for energy storage devices and electron microscopy/spectroscopy characterization of battery materials.

Professor Jiaxin Zheng received his BSc in Physics in 2008 and PhD degree in Condensed Matter Physics in 2013 from Peking University, China. Then he joined the group of Prof. Feng Pan at School of Advanced Materials (SAM), Peking University, Shenzhen Graduate School, China, as a post-doctoral fellow from Oct. 2013 to Oct. 2015. Now he works an associate Professor at SAM. His research interests include: computational materials, energy materials (battery materials, solar energy, thermoelectric materials), nanomaterials, nanoelectronics. Dr. Zheng has authored/co-authored more than 80 peer-reviewed research articles.

Professor Yuan Lin, Institute of Chemistry, Chinese academy of Sciences, born in 1964, got B.S. from Dept. Chemistry, Peking University in1985 , M.S. and PhD from Chinese Academy of Sciences (CAS) in 1988 and 1995 respectively. In 1988–1999, he took the position of assistant professor in Institute of photographic Chemistry, Chinese academy of Sciences. From 1999 to present, he took the position of professor. For more than 20 years, Prof. Lin has been engaged in the fields of photoelectrochemical conversion of solar energy, preparation of nanocrystalline semiconductors, investigation of photoelectrochemical and surface properties of nanocrystalline semiconductors, developing ionic liquid and polymeric materials for electrolytes.

Professor Feng Pan, founding Dean of School of Advanced Materials, Peking University Shenzhen Graduate School, got B. S. from Dept. Chemistry, Peking University in 1985 and Ph.D. from Dept. of P&A Chemistry, University of Strathclyde, Glasgow, UK, with "Patrick D. Ritchie Prize" for the best pH. D. in 1994. With more than a decade experience in large international incorporations, Prof. Pan has been engaged in fundamental research and product development of novel optoelectronic and energy storage materials and devices. As Chief Scientist, Prof. Pan led eight entities in Shenzhen to win the 150 million RMB grant for the national new energy vehicles (power battery) innovation project since 2013.